PAPER

Check for updates

Kinetic interface design in carbon-doped Mg(OH)$_2$ enables concurrent CO$_2$ blocking and capture

Hashan N. Thenuwara, [ID] [ab] W. P. Cathie Lee, [ID] [a] Shunnian Wu, [a] Sim Jia Yu, [b] Siew Yee Wong, [ID] [b] Xu Li*[b] and Ping Wu [ID] *[a]

In this study, we report a kinetically engineered Mg(OH)$_2$-based nanostructure that simultaneously blocks carbonate passivation and contributes to CO$_2$ capture. The material was synthesized *via* a non-equilibrium spray drying process followed by calcination at 350 °C and facile steam treatment producing carbon-doped MgO–Mg(OH)$_2$ nanoparticles with a dual-function interfacial architecture. While conventional Mg(OH)$_2$ regions can mitigate MgCO$_3$ formation by acting as CO$_2$ diffusion barriers, they consume active MgO, thereby lowering overall sorbent capacity. Here, carbon doping transforms the role of Mg(OH)$_2$: it not only limits carbonate growth but also introduces oxygen vacancies and defect sites that actively adsorb CO$_2$. The non-equilibrium kinetically driven conditions of spray drying kinetically trap carbon species near the surface, forming self-limiting, carbon-rich Mg(OH)$_2$ regions around reactive MgO domains. This architecture achieves a CO$_2$ uptake of 5.45 wt% at room temperature with a low regeneration temperature of 150 °C, despite having a lower surface area than its undoped counterpart. Cyclic tests revealed 62% capacity retention after five regeneration cycles at 150 °C, owing to gradual active site saturation. These findings demonstrate that controlled carbon enrichment and defect engineering in Mg(OH)$_2$ unlock its dual role, acting both as a protective interface and as a reactive sorbent, enabling efficient and regenerable CO$_2$ capture.

1. Introduction

The escalating impacts of climate change, evidenced by extreme weather events like heatwaves and flooding, highlight the urgency to reduce CO$_2$ emissions, primarily driven by fossil fuel combustion.[1–3] The Paris Agreement emphasizes limiting global temperature rise to 1.5 °C through a broad range of actions to reduce greenhouse gas emissions, including carbon adsorption.[4] Conventional methods, such as aqueous amine solutions, are effective but energy-intensive and costly due to high regeneration requirements.[5–7] In contrast, solid sorbents like magnesium oxide (MgO) offer promising advantages, including lower regeneration temperatures, enhanced durability, and scalability.[8,9] The abundance, high theoretical CO$_2$ capture capacity, and favorable adsorption properties of MgO make it an economical and effective choice.[10,11]

However, there are certain challenges associated with MgO as a CO$_2$ capture sorbent, including its low practical CO$_2$ capture capacity and poor sorption kinetics, primarily attributed to the scarcity of active basic sites.[8,12] Furthermore, the chemical adsorption of CO$_2$ onto the surface of MgO leads to the formation of a MgCO$_3$ layer, which blocks CO$_2$ from diffusing into the MgO core, ultimately reducing the CO$_2$ capture efficiency below its theoretical maximum.[8,13] To address this limitation, our group previously demonstrated a novel strategy by developing a CO$_2$-phillic MgO and CO$_2$-phobic Mg(OH)$_2$ binary system through a combined electrospinning and steaming process, which effectively suppressed the formation of the MgCO$_3$ shell layer, thereby enhancing CO$_2$ adsorption capacity.[11,13] While this binary strategy is effective in suppressing carbonate passivation, it inherently consumes a portion of MgO to form Mg(OH)$_2$, thereby reducing the net CO$_2$ capture efficiency when normalized to the initial Mg content. Hence, to further enhance CO$_2$ adsorption, we have developed a new strategy which allows Mg(OH)$_2$ regions to contribute to CO$_2$ adsorption.[14] It has been recently reported that carbon doping significantly enhances CO$_2$ adsorption in MgO by increasing electron donation capacity and surface interaction strength, outperforming other high valence dopants in adsorption energy. Therefore, we utilized carbon doping into both MgO and Mg(OH)$_2$ phases through a spray drying synthesis method, which is a scalable and straightforward synthesis method capable of introducing lattice defects

[a] Entropic Interface Group, Engineering Product Development, Singapore University of Technology and Design, 8 Somapah Road, 487372, Singapore. E-mail: wuping@sutd.edu.sg

*[b] Institute of Materials Research and Engineering, Agency for Science, Technology and Research (A*STAR), Fusionopolis Way, Innovis, 138634, Singapore. E-mail: x-li@imre.a-star.edu.sg*

in MgO.[15] The rapid solvent evaporation and non-equilibrium conditions during spray drying could also facilitate the entrapment of carbon species within the MgO and $Mg(OH)_2$ lattice structures.

Also, achieving low regeneration temperatures is crucial for reducing the energy requirements of CO_2 capture processes. Our previous studies have demonstrated the effectiveness of MgO-based adsorbents regenerated at 150 °C using various synthesis methods. For example, electrospun MgO–$Mg(OH)_2$ exhibited a CO_2 uptake of 4.12 wt%,[16] Cl^--doped MgO–$Mg(OH)_2$ achieved 4.59 wt%,[17] and freeze-dried MgO–$Mg(OH)_2$ reached 6.2 wt%.[18]

In this study, we present a novel strategy to mitigate the carbonate-blocking effect on MgO during CO_2 adsorption by employing kinetically engineered carbon-doped MgO–$Mg(OH)_2$ binary nanostructures. MgO-based nanoparticles were synthesized via a spray drying method, followed by steam treatment to graft flower-like MgO–$Mg(OH)_2$ binary architectures. Previous studies have shown that $Mg(OH)_2$ domains in MgO–$Mg(OH)_2$ composites suppress carbonate passivation by serving as CO_2-phobic layers, but this comes at the expense of consuming active MgO. In this study, we demonstrate that carbon doping completely redefines this role: $Mg(OH)_2$ is no longer only a diffusion barrier but also functions as a defect-rich sorption phase, actively contributing to CO_2 capture via oxygen vacancy sites. This dual-function transformation of $Mg(OH)_2$ represents a key advancement in Mg-based sorbents. The morphological and structural characteristics, along with CO_2 adsorption performance, were systematically investigated. Furthermore, first-principles calculations were conducted to elucidate the effects of carbon doping on the binary system. This approach offers valuable insights for advancing CO_2 capture technologies and, we believe, merits the attention of the broader research community.

2. Experimental

2.1 Materials

Magnesium acetate tetrahydrate ($Mg(CH_3COO)_2 \cdot 4H_2O$) (ACS reagent, ≥98%) and poly(vinyl alcohol) (M_w 30 000–50 000, 87–90% hydrolyzed) were purchased from Sigma Aldrich. MgO nanopowder (extra pure) was acquired from GCE chemicals. All chemicals were used as received without further purification. Deionized water was supplied by a Neptec Halios lab water system.

2.2 Synthesis of MgO–$Mg(OH)_2$ binary nanoparticles

To synthesize MgO–$Mg(OH)_2$ nanoparticles, $Mg(CH_3COO)_2 \cdot 4H_2O$ was dissolved in DI water to prepare 40 g L^{-1} precursor solution and kept stirring for 2 h until a clear solution was obtained. It was fed into a spray dryer machine at a flowrate of 10 mL min^{-1} and an evaporation temperature of 220 °C. Then, the spray dried (SD) powder was calcined in a muffle furnace at 350 °C for 1 h with a ramp rate of 2 °C min^{-1} and naturally cooled down to room temperature to obtain MgO powder. To obtain MgO–$Mg(OH)_2$

nanocomposite particles, prepared MgO powder was further steamed using a steam oven at 100 °C for 20 minutes. To synthesize the spray dried carbon doped MgO–$Mg(OH)_2$ nanopowder, 4 wt% polyvinyl alcohol was added to a magnesium acetate tetrahydrate solution to prepare a 40 g L^{-1} spray-drying solution following the same procedure as above.

2.3 Characterization

The surface morphology was analyzed using a field emission scanning electron microscope (FESEM) (JEOL JSM-7600F, Jeol, Tokyo, Japan), while an X-ray diffractometer (Bruker D8 Advance) with Cu-K radiation (λ = 1.54 Å) was employed to obtain XRD spectra. The analysis of specific surface areas and micropore volumes was conducted using a Micrometrics ASAP 2020 Brunauer–Emmett–Teller (BET) system. Prior to the BET tests, the samples were subjected to a degassing process at 200 °C for 15 hours. The CO_2 capture capacity was determined using a thermogravimetric analysis (TGA) Q50 analyzer (TA Instruments, New Castle, DE, USA). Prior to TGA, samples were subjected to a preliminary step of thermal treatment for 60 minutes at 150 °C with a high-quality N_2 gas flow of 40 mL min^{-1}. This step aimed to eliminate preabsorbed moisture and other impurities from the environment during storage. Subsequently, high-quality CO_2 gas was introduced for a predetermined duration at 30 °C and 40 mL min^{-1}. The increase in the sample weight during CO_2 gas exposure was utilized to calculate the CO_2 capture capability. The carbon content of the doped samples was determined using a Thermo Scientific Flash EA 1112 Series CHNS-O analyzer. Surface basicity and defect site characteristics were evaluated by CO_2 temperature-programmed desorption (CO_2-TPD) using a Micromeritics AutoChem II 2920 system. Samples were first pretreated at 150 °C for 30 minutes under a nitrogen atmosphere to remove surface-bound impurities. CO_2 adsorption was then carried out at room temperature for 1 hour using pure CO_2 gas, followed by desorption under N_2 flow while heating the samples from room temperature to 900 °C at a ramp rate of 10 °C min^{-1}.

The average crystallite size of the samples was estimated using the Debye–Scherrer equation:

$$D = \frac{K\lambda}{\beta \cos \theta} \qquad (1)$$

where D is the crystallite size, K is the shape factor (taken as 0.9), λ is the wavelength of $CuK\alpha$ radiation, β is the full width at half maximum (FWHM) of the diffraction peak, and θ is the Bragg angle.

To further analyze the structural parameters, the Williamson–Hall (W–H) method was employed to evaluate both lattice strain and dislocation density. The W–H equation is expressed as

$$\beta \cos \theta = \frac{K\lambda}{D} + 4\varepsilon \sin \theta \qquad (2)$$

where ε represents the microstrain. A plot of $\beta \cos \theta$ versus $4 \sin \theta$ was constructed, and the crystallite size was obtained from the y-intercept, while the slope provided the strain values.

From the calculated crystallite size and strain, the corresponding dislocation density (δ) was further estimated using

$$\delta = \frac{1}{D^2} \qquad (3)$$

This combined Scherrer and W–H analysis provides complementary insights into the crystallite size, lattice strain, and defect density within the synthesized nanostructures.

2.4 Computational details

The first-principles calculations were performed using periodic models with the Vienna *ab initio* simulation package (VASP).[19] Geometry optimizations were carried out employing the general gradient approximation (GGA) Perdew–Burke–Ernzerhof (PBE) exchange–correlation functional.[20] A projector augmented wave (PAW) method[21,22] was applied as a plane wave basis and the kinetic energy cutoff for the plane-wave expansion was set at 500 eV. The DFT+D3 correction[23] is incorporated with the PBE functional to take into consideration the van der Waals contribution. For geometry optimization and total energy calculations, the total energy convergence was set to 1.0×10^{-6} eV, and the force on each individual atom was minimized to be smaller than 0.01 eV Å^{-1}. The value for smearing was fixed to 0.01 eV. The Brillouin zone was sampled using the Monkhorst–Pack K-point mesh technique[24] with the K-point number (N_K) being adjusted to keep $N_K \times L$ (L is the lattice constant) equal to $\sim$25 Å. The previously obtained MgO and Mg(OH)$_2$ crystalline structures[25,26] were used in this study. A neutral vacancy was generated by removing one atom from the $3 \times 3 \times 3$ MgO or $4 \times 4 \times 3$ Mg(OH)$_2$ supercell, which yields the vacancy concentration of about 0.4%. The vacancy formation energy E_f is defined as $E_f = E_0 - E_v - \mu_i$, where E_0 and E_v are the total energy of the perfect structure and that of the neutral defective structure, respectively. μ_i is the chemical potential of the atom participating in the defect. This reference energy is taken as the energy of that atom in its most stable ground-state structure, *e.g.*, we used the O$_2$ molecule in its triplet state as the reference for the O atom. Vacancy formation energy is the amount of energy required to create a vacancy defect in a crystal lattice, *i.e.*, to remove an atom from its regular site in the lattice. It quantifies the energy cost for a material to have a missing atom, determines the concentration of vacancies at a given temperature (*via* thermodynamics) and influences material properties such as diffusion, conductivity, and mechanical strength.

3. Results and discussion

The morphologies of the samples were characterized through SEM, and Fig. 1(a) and (b) present the SEM images of pristine and carbon doped MgO–Mg(OH)$_2$ nanoparticles. Clearly visible in these images is the flake-like structure grafted onto the surface of the MgO nanoparticles through the steaming process, resulting in a distinctive flower-like arrangement. To confirm the presence of MgO–Mg(OH)$_2$ binary phases in the nanoparticle structure, XRD analysis (Fig. 2) was conducted for both binary nanoparticle samples. The peaks corresponding to MgO at 42.9° and 62.3° align with lattice planes (200) and (220), respectively, consistent with MgO (ICDD 00-045-0946). The Mg(OH)$_2$ peaks formed after steaming, specifically at 18.5°, 32.8°, 37.9°, 50.7°, 58.6° and 68.1°, correlate with (001), (100), (101), (102), (110) and (103) lattice planes, respectively, showing good agreement with Mg(OH)$_2$ (ICDD 00-044-1482). SEM imaging and XRD analysis of the carbon-doped spray-dried hybrid samples revealed a flower-like morphology and lattice structure consistent with undoped samples, indicating that carbon doping does not alter the morphological transformation. The carbon content in the carbon doped SD binary MgO–Mg(OH)$_2$ sample was determined to be 5.27% using CHNS analysis. The non-equilibrium kinetic conditions were introduced specifically during spray drying, in which the rapid solvent evaporation and local supersaturation lead to incomplete decomposition of the carbon precursor and its entrapment near the Mg precursor
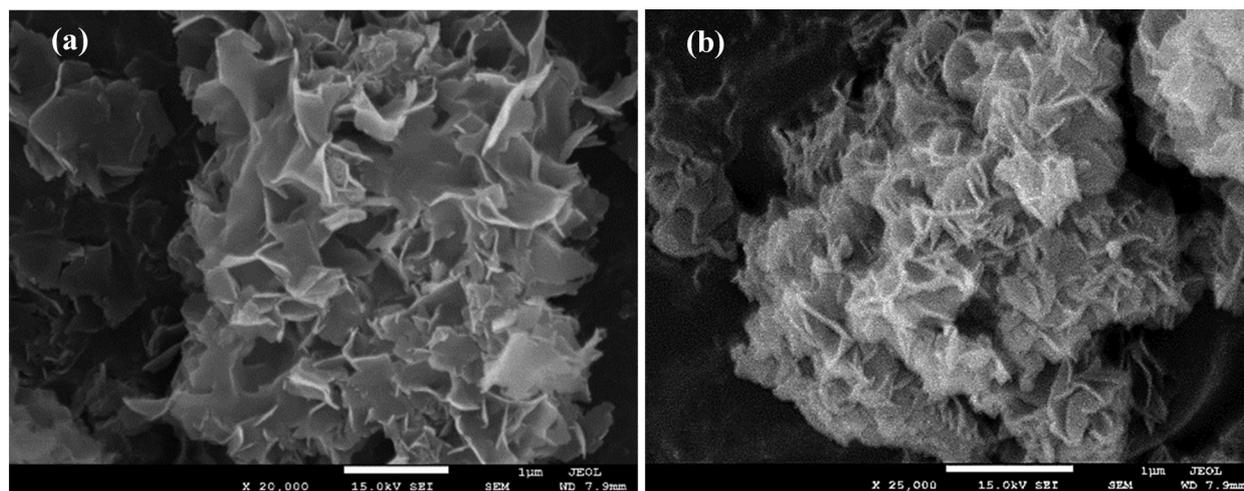

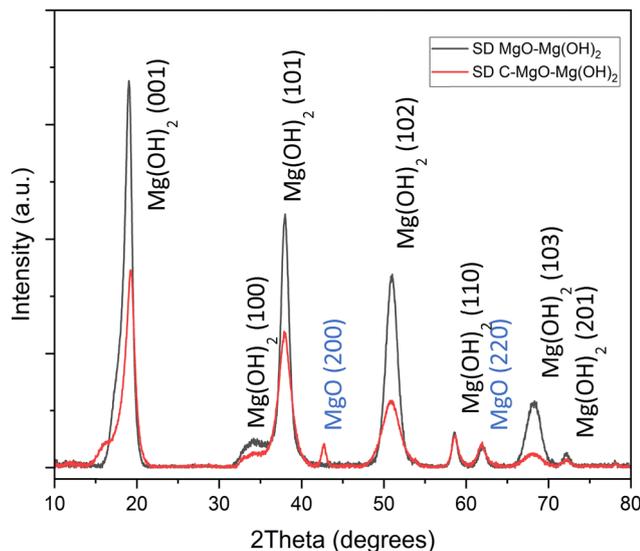**Fig. 1** SEM images of MgO–Mg(OH)$_2$ nanoparticles: (a) undoped and (b) carbon-doped samples.

Fig. 2 XRD patterns of spray-dried MgO–Mg(OH)$_2$ nanoparticles.

matrix. These subsequent calcination and steaming steps stabilize the kinetically trapped carbon within the MgO and Mg(OH)$_2$ lattice or interfacial regions.

Interestingly, the X-ray diffraction (XRD) patterns of spray-dried MgO–Mg(OH)$_2$ nanocomposites exhibited an unusual intensity trend, with a monotonic decrease in peak intensity from low to high 2θ angles and a dominant (001) reflection. This contrasts sharply with the more uniform intensity distributions observed in samples prepared *via* electrospinning in our previous work[16] and other conventional methods. The observed intensity gradient is attributed to a pronounced preferred orientation of the Mg(OH)$_2$ phase, which adopts a brucite-type hexagonal layered structure known to promote anisotropic growth into thin, flake-like morphologies. Such orientation behavior is characteristic of 2D layered materials like graphene oxide,[27] boron nitride,[28] and MOS$_2$,[29] where basal plane reflections dominate due to strong in-plane interactions and stacked out-of-plane arrangements.

The dominant (001) reflection observed in the spray-dried Mg(OH)$_2$ phase corresponds to basal-plane stacking, which exposes large interlayer galleries along the layer stacking direction. These galleries act as diffusion channels and confinement pockets during spray drying, allowing decomposed carbonaceous fragments from the precursor (polyvinyl alcohol) to diffuse into and become confined within the structure. During subsequent calcination and hydration, these species are kinetically trapped within interlayer sites or at domain boundaries, resulting in interstitial incorporation of carbon.

The monotonic decrease in peak intensity at higher angles is consistent with this preferred orientation. In highly oriented systems, reflections corresponding to planes other than (001) are significantly suppressed, leading to a relative enhancement of the (001) peak and diminished intensities at higher 2θ values. This effect reflects both the textural anisotropy of the spray-dried Mg(OH)$_2$ platelets and the increased disorder introduced by intercalated carbon, which broadens and weakens higher-order reflections. Thus, the dominant (001) orientation not only provides the structural channels that facilitate carbon incorporation but also accounts for the systematic reduction in higher-angle peak intensities. Additionally, the observed broadening of the full width at half maximum (FWHM) in the XRD peaks of the carbon-doped MgO–Mg(OH)$_2$ nanocomposites further validates that carbon incorporation introduces structural disorder and defect formation due to interstitial entrapment of carbon species within the binary structure.[14]

The crystallite size and lattice strain contributions of Mg(OH)$_2$ were further examined using the Williamson–Hall (W–H) method. The results are summarized in Table 1. Compared to pristine Mg(OH)$_2$, the carbon-doped Mg(OH)$_2$ sample exhibited a smaller crystallite size, decreasing from 4.72 nm to 3.78 nm (W–H method). This reduction in the crystallite size indicates that carbon incorporation inhibits grain growth during synthesis, leading to a higher density of grain boundaries. In addition, the microstrain increased significantly in the carbon-doped sample (from −0.0052 to −0.0079), suggesting that carbon entrapment induces additional lattice distortion and defect formation within the Mg(OH)$_2$ structure. Consistently, the calculated dislocation density rose from 4.49 × 10^{16} m^{-2} in pristine Mg(OH)$_2$ to 6.98 × 10^{16} m^{-2} in the doped sample, confirming a higher concentration of crystallographic imperfections. Together, these results support that carbon doping introduces considerable lattice strain and defect density, which can act as additional active sites for CO$_2$ binding.

Thermogravimetric analysis (TGA) was performed to assess the CO$_2$ adsorption capacities of MgO and binary MgO–Mg(OH)$_2$ nanoparticles. The undoped binary MgO–Mg(OH)$_2$ samples (Fig. 3(a)) exhibited a higher CO$_2$ adsorption during the initial 50 minutes, followed by a decline in uptake compared to the undoped MgO sample. The elevated initial CO$_2$ uptake observed in the undoped MgO–Mg(OH)$_2$ binary system originates primarily from the presence of Mg(OH)$_2$ layers, which act as diffusion channels that accelerate CO$_2$ transport and capture during the early adsorption stage.[13] In addition, the spray-dried MgO–Mg(OH)$_2$ exhibits a flake-like morphology with interwoven MgO and Mg(OH)$_2$ regions, which further enhances gas transport kinetics. This hierarchical morphology

Table 1 Williamson–Hall crystallite size and lattice microstrain analysis

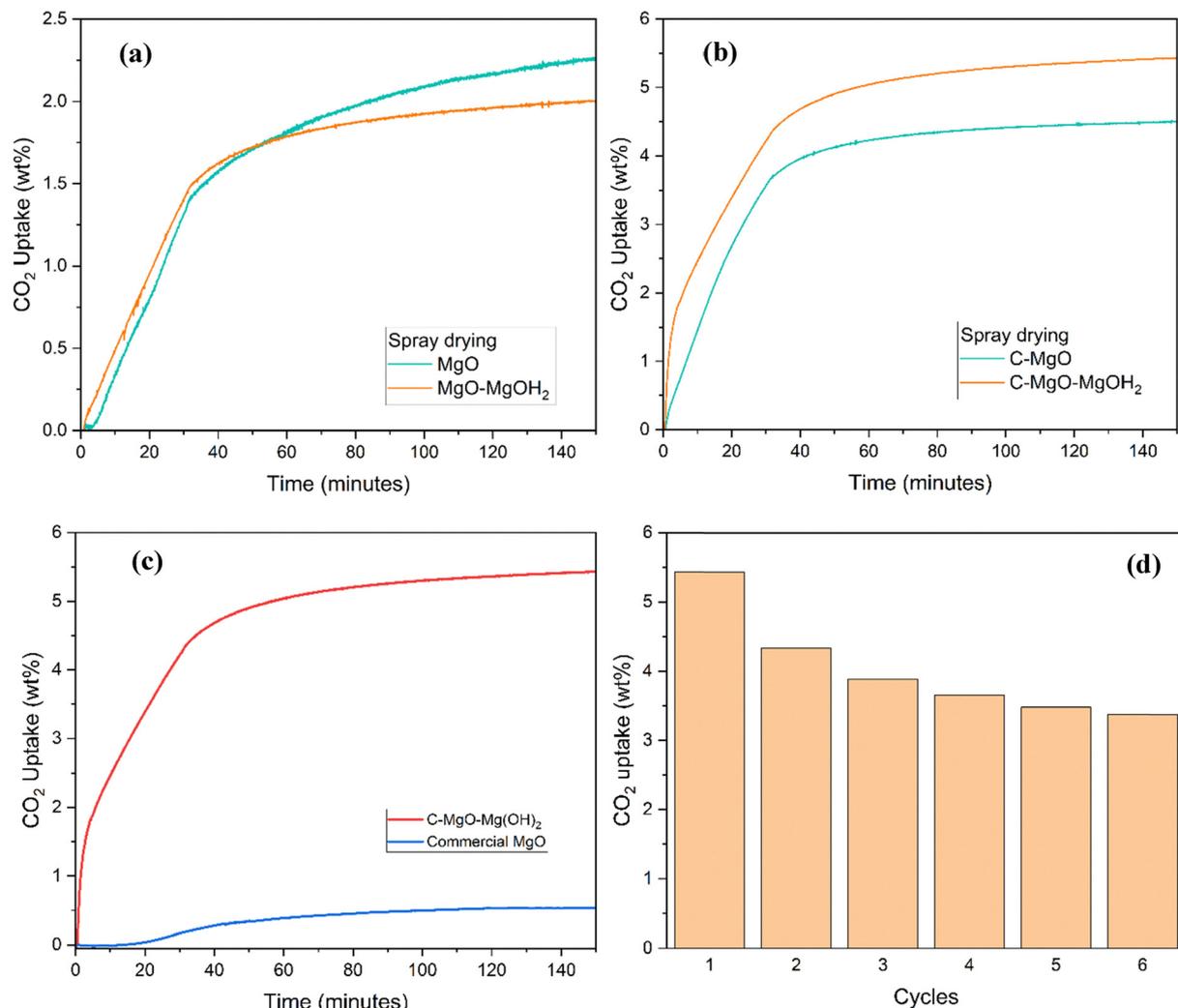|	Crystallite size (nm) (Scherrer equation)	Crystallite size (nm) (W–H method)	Microstrain (× 10^{-3}) (W–H method)	Dislocation density (× 10^{16}) (m^{-2}) (W–H method)
Pristine Mg(OH)$_2$	7.297	4.716	−5.243	4.49
C-doped Mg(OH)$_2$	6.532	3.784	−7.883	6.98

Fig. 3 CO$_2$ adsorption performance of (a) undoped MgO and binary MgO–Mg(OH)$_2$ and (b) C−MgO and binary C−MgO−Mg(OH)$_2$; (c) comparative CO$_2$ uptake of C−MgO−Mg(OH)$_2$ and commercial MgO; and (d) cyclic performance of C−MgO−Mg(OH)$_2$.

collectively contributes to the higher initial CO$_2$ uptake rates of the binary system compared to MgO alone.

However, this binary architecture inherently consumes a portion of MgO to form Mg(OH)$_2$. As the CO$_2$ capture reaction progresses, MgO is progressively consumed through the formation of MgCO$_3$, eventually leading to complete conversion of the available MgO within the undoped binary structure. In contrast, pristine MgO, though exhibiting a slower initial uptake, achieves a higher overall capacity due to its larger fraction of CO$_2$-philic active sites compared to the pristine binary sample. In contrast, carbon doped binary MgO–Mg(OH)$_2$ showed significantly higher CO$_2$ adsorption from the beginning to end. This enhancement is likely to be attributed to carbon interstitial defects introduced into the binary nanostructure during synthesis.

The carbon-doped binary nanoparticles achieved the highest CO$_2$ uptake of 5.45 wt%, more than 2.7 times of the undoped binary sample. In comparison, commercial MgO exhibited a CO$_2$ capture performance of only 0.56 wt% under the same conditions. All the CO$_2$ adsorption experiments were repeated three times, and the calculated standard deviation across the repeated measurements was <1%, demonstrating high reproducibility. Additionally, Table T1 (SI) compares the performance of the present sorbent with that of reported MgO-based systems. Furthermore, the CO$_2$-TPD results revealed a total desorption of 65 wt% (14.9 mmol g^{-1}), indicating that the sample had already chemisorbed a substantial amount of CO$_2$ from the ambient environment during handling and storage. This behavior suggests the presence of abundant, strongly interacting adsorption sites capable of capturing CO$_2$ even at very low partial pressures.

Cyclic CO$_2$ capture performance of C−MgO−Mg(OH)$_2$ was also evaluated over six cycles, with regeneration at 150 °C for 60 minutes between cycles. As shown in Fig. 3(d), CO$_2$ uptake decreased from 5.45 wt% to 3.37 wt% after six cycles, likely due to incomplete conversion of MgCO$_3$ back to MgO at the relatively low regeneration temperature (150 °C) employed. This suggests that the spray-dried samples utilize both chemical and

physical adsorption mechanisms for CO_2 capture, consistent with mechanisms proposed in a previous study.[18] As observed from CO_2-TPD studies (Fig. 6), raising regeneration temperature (350–400 °C) would not only enhance recovery but also increase energy penalty, thereby lowering net process efficiency. However, regeneration temperature plays a critical role in preserving the MgO–Mg(OH)$_2$ binary structure. Thermodynamically, Mg(OH)$_2$ undergoes endothermic decomposition to MgO and H$_2$O. This transformation typically initiates at $\sim$350 °C and becomes complete above $\sim$400–420 °C, driven by increases in Gibbs free energy (ΔG), favoring the oxide phase at higher temperatures. While higher regeneration temperatures improve desorption of strongly bound CO_2 species, operating above 400 °C leads to full dehydroxylation and permanent loss of the Mg(OH)$_2$ phase. This would eliminate the CO_2-phobic transport domains essential for mitigating $MgCO_3$ shell formation and would require an additional rehydration/steaming step to restore the binary structure before the next adsorption cycle. Therefore, regeneration at 150 °C provides a balance between energy efficiency and structural preservation.

Table 2 presents a comprehensive summary of the textural characteristics of the MgO–Mg(OH)$_2$ binary nanoparticle samples, derived from BET surface area analysis. Fig. 4 presents the N$_2$ adsorption–desorption isotherms and according to the IUPAC classification, both the spray-dried nanoparticles fall into the mesoporous category, characterized by pores ranging from 2 to 50 nm. The undoped spray-dried samples exhibited a significantly higher surface area and smaller pore sizes. However, after carbon incorporation, the surface area of the spray-dried samples decreased from 62.3 m^2 g^{-1} to 46.4 m^2 g^{-1}.

Fig. 5 presents the FTIR spectra of the undoped MgO–Mg(OH)$_2$ and carbon-doped MgO–Mg(OH)$_2$ samples. Both materials exhibit the characteristic vibrational features of brucite-like Mg(OH)$_2$ and MgO; however, clear differences arise upon carbon incorporation. The broad absorption band in the 3000–3600 cm^{-1} region corresponds to O–H stretching modes of surface hydroxyls and hydrogen-bonded water, while the sharp peak at 3697 cm^{-1} is attributed to the stretching vibration of structural Mg–OH groups.[18,30] In contrast, the carbon-doped sample exhibits systematically reduced intensities and a lowered baseline across the hydroxyl region. The attenuation of O–H and Mg–OH vibrational features suggests that carbon incorporation decreases the density of free surface hydroxyls—likely through partial occupation of interlayer or near-surface sites or through the formation of Mg–C/Mg–O–C linkages that disrupt hydroxyl coordination. Similar reductions in overall peak intensities in doped MgO systems have been reported by Sikdar et al. and Subash et al.[31,32] In the mid-infrared region ($\approx$1250–1650 cm^{-1}), the undoped sample also displays more
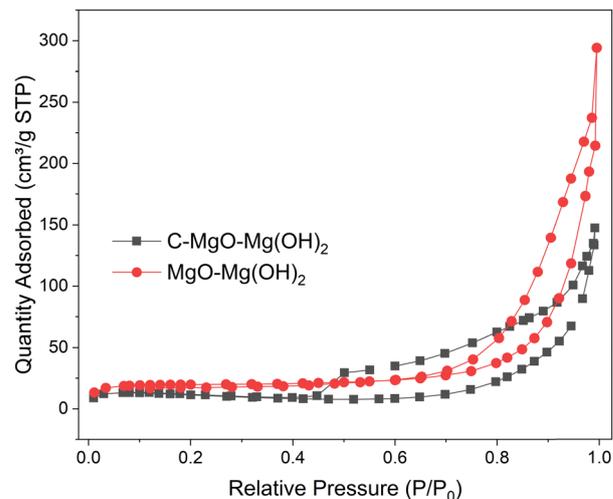

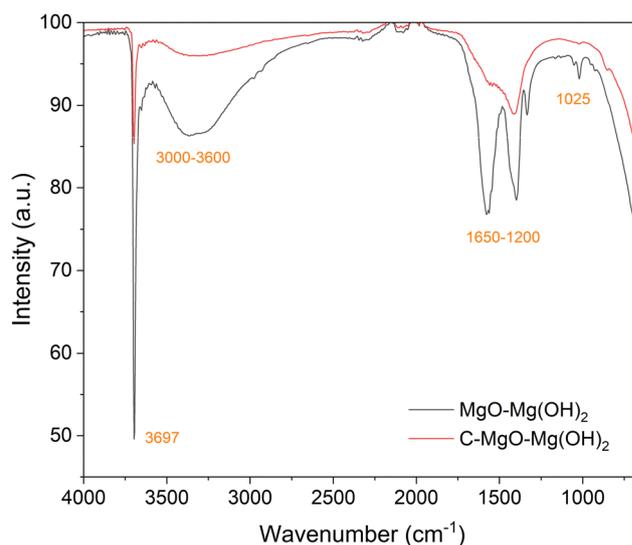Fig. 4 N$_2$ adsorption–desorption isotherms of spray-dried MgO–Mg(OH)$_2$ nanoparticles.

Fig. 5 FTIR spectrums of spray-dried MgO–Mg(OH)$_2$ nanoparticles.

pronounced H–O–H bending and carbonate-related bands[33] compared to the doped sample, reflecting greater physisorbed water and carbonate accumulation on its higher-surface-area structure. The band in the 900–1100 cm^{-1} region is attributed to Mg–O–H deformation/formation of surface bicarbonate species[34,35] and is present in both materials; however, the diminished intensity and subtle band-shape modifications in the doped sample suggest increased structural disorder within the local Mg–OH environment induced by carbon incorporation.

To investigate the surface defect states of C–MgO and assess the distribution of basic site strengths, CO_2 temperature-programmed desorption (CO_2-TPD) was performed on the C–MgO–Mg(OH)$_2$ sample after CO_2 adsorption at room temperature. As shown in Fig. 6, the CO_2-TPD profile reveals four

Table 2 Textural properties of binary nanoparticle samples

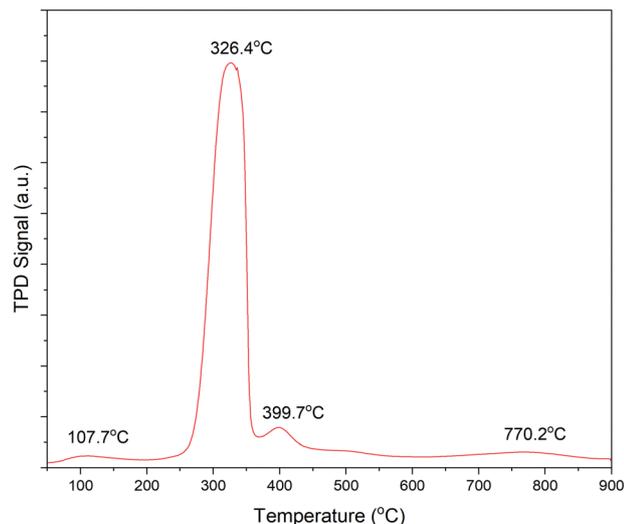| Sample	Surface area (m^2 g^{-1})	Pore size (nm)	Pore volume (cm^3 g^{-1})
Undoped MgO–Mg(OH)$_2$	62.36	10.42	0.174
Carbon-doped MgO–Mg(OH)$_2$	46.46	19.63	0.228

Fig. 6 CO_2-TPD profile of the carbon doped MgO–Mg(OH)$_2$ sample.

distinct desorption peaks at 107.7 °C, 326.4 °C, 399.7 °C, and 770.2 °C. The desorption temperatures indicate the binding strengths of CO_2 at different adsorption sites, while the corresponding peak areas reflect the relative concentration of these basic sites. These sites can be broadly classified into three categories.[18,36,37] The weak basic sites (<200 °C), represented by the peak at 107.7 °C, arise from CO_2 weakly interacting with the Mg(OH)$_2$ phase, forming bicarbonates through reactions with surface –OH groups. Medium basic sites (200–300 °C), typically associated with bidentate carbonates stabilized at Mg^{2+}–O^{2-} surface pairs, were not detected in this study. The strong basic sites (>300 °C) are indicated by the peaks at 326.4 °C and 399.7 °C, which correspond to strongly bound carbonate species, typically monodentate carbonates stabilized at low-coordination O^{2-} sites. Compared to other categories of basic sites, these peaks exhibit the highest intensities, suggesting a high density of low-coordination O^{2-} sites in the C–MgO–Mg(OH)$_2$ samples. This observation is consistent with the first-principles calculations reported by Wu *et al.*, which demonstrated that carbon doping redistributes electrons near defect sites, thereby generating additional low-coordination O^{2-} species.[14]

Notably, the high-temperature peak at 770.2 °C is attributed to very strongly bound carbonates, likely bidentate or tridentate species stabilized in vacancy-related environments, such as F-centers and defect clusters. In this system, these features are plausibly linked to oxygen vacancies induced by carbon doping. Such vacancy defects can donate electrons into the antibonding orbitals of CO_2, thereby increasing the electron density at the adsorbent surface and strengthening CO_2 binding.[18,38,39] In addition, neighboring metal cations adjacent to vacancy sites can further facilitate electron transfer to the oxygen atoms of CO_2 molecules.[40] The high binding energies associated with these defect-rich environments hinder CO_2 desorption, accounting for the strong high-temperature peak observed at 770.2 °C in the CO_2-TPD profile.

The XPS analysis (Fig. 7) confirmed the presence of Mg, O and C as the major elements in the carbon doped MgO–Mg(OH)$_2$ sample. The high-resolution Mg 1s spectrum exhibits a dominant peak at 1305 eV, characteristic of Mg^{2+} in MgO, indicating that magnesium is primarily present in an oxidized lattice environment. The C 1s spectrum was deconvoluted into three distinct peaks centered at 280.4, 284.8, and 288.9 eV. The prominent peak at 284.8 eV is attributed to graphitic or adventitious carbon (C–C/C–H), while the high-binding-energy component at 288.9 eV corresponds to carbonate (CO_3^{2-}) or oxygenated carbon species (C=O/C–O) formed during synthesis or air exposure. Crucially, the low-binding-energy feature at 280.4 eV is assigned to C–Mg bonding, indicating that carbon atoms are chemically incorporated into the Mg–O lattice, most likely substituting for oxygen or forming interfacial Mg–C bonds. This observation confirms that carbon exists not only as surface adsorbates but also as lattice-stabilized dopant species. The O 1s spectrum was deconvoluted into three components centered at 529.5, 531.0, and 532.0 eV, corresponding to lattice oxygen, oxygen deficiency, and hydroxyl oxygen, respectively.[18,41] The dominance of the O_{II} component (77.1%) indicates a high concentration of oxygen vacancy defects in carbon doped MgO–Mg(OH)$_2$, which are consistent with lattice distortion induced by carbon incorporation.

Table 3 summarizes the calculated formation energy of the O vacancy in MgO and the OH vacancy in Mg(OH)$_2$, respectively. Our preliminary calculations indicate that the formation energy (E_f) of the Mg vacancy is more than 2.0 eV higher than that of the O vacancy in MgO and more than 3.0 eV higher than that of the OH vacancy in Mg(OH)$_2$, and therefore, the Mg vacancy is not considered in this study. The significantly higher vacancy formation energy for Mg compared to O or OH vacancies may be due to the strong Madelung contribution associated with the cation sites. In Mg(OH)$_2$ or MgO, Mg^{2+} cations play a critical role in maintaining the overall charge neutrality and lattice stability. The removal of a Mg^{2+} cation generates a highly unstable negatively charged environment, which cannot be easily compensated by neighboring ions, thereby inducing large lattice distortions. This destabilization makes Mg vacancy formation energetically unfavorable. In contrast, the removal of O^{2-} or OH^- anions can be more effectively stabilized by the surrounding Mg^{2+} cations. Local lattice relaxation and electronic redistribution mitigate the destabilization, thereby lowering the vacancy formation energy. Our formation energy of the O vacancy in pristine bulk MgO is consistent with the reported formation energy of 6.27 eV for the O vacancy on the MgO (001) surface.[42] It can be seen from Table 2 that the formation energy

Table 3 Calculated E_f of the O vacancy in MgO and the OH vacancy in Mg(OH)$_2$

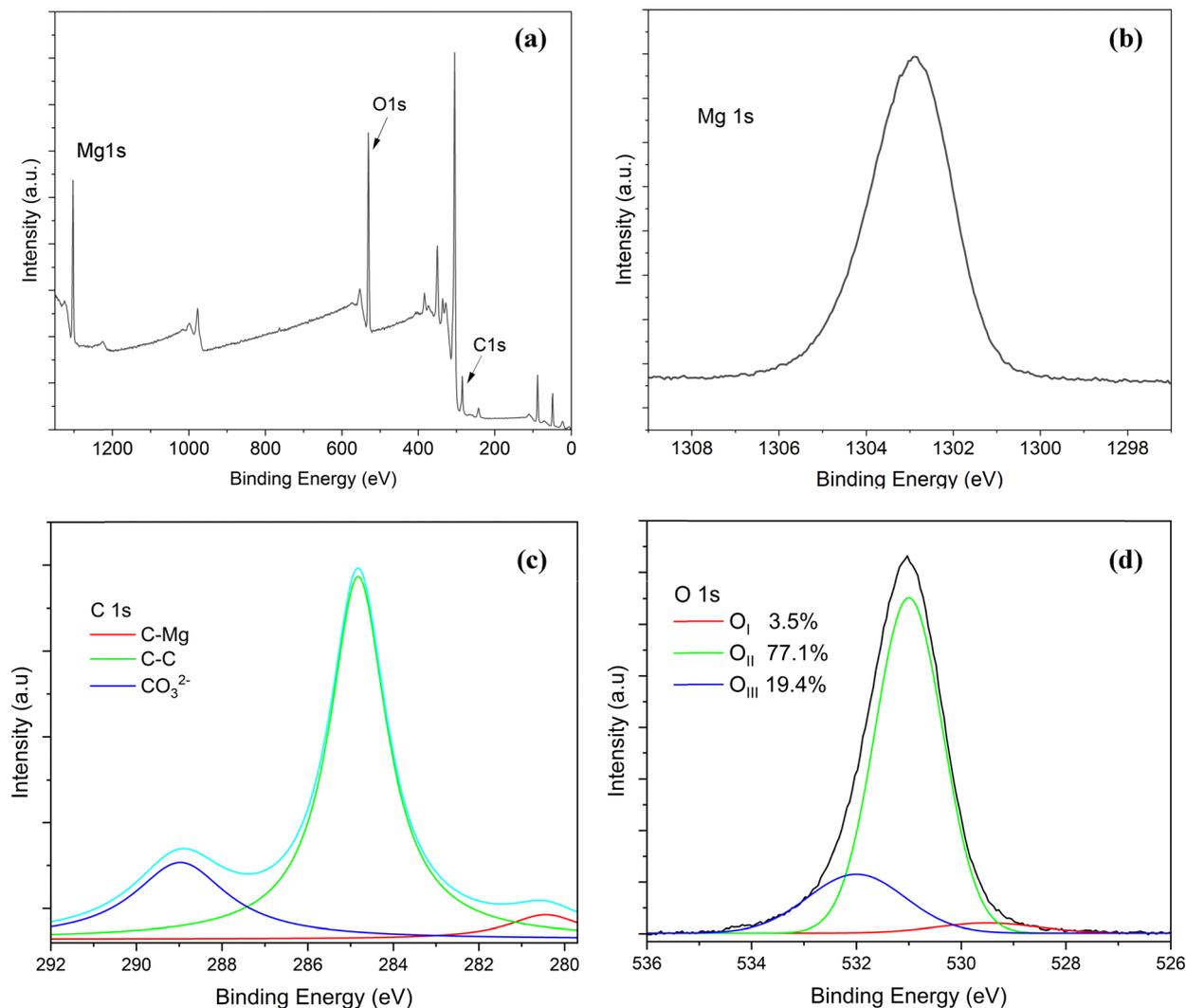| Structure	E_f (eV)
Pristine MgO	6.70
MgO with interstitial C	2.08
Pristine Mg(OH)$_2$	5.85
Mg(OH)$_2$ with interstitial C	2.30

Fig. 7 XPS analysis of the carbon-doped MgO–Mg(OH)$_2$ sample: (a) survey spectrum and high-resolution spectra of (b) Mg 1s, (c) C 1s, and (d) O 1s.

of the OH vacancy is about 13% lower than that of the O vacancy for both the pristine samples. In our study, the hydration of MgO to form Mg(OH)$_2$ provides another approach to increase the vacancy concentration.

Notably, the insertion of an interstitial C atom significantly reduces the formation energy of the O vacancy of MgO by approximately 70%. This indicates that doping is a highly effective strategy for significantly increasing the concentration of O vacancies. Additionally, the insertion of an interstitial C atom into Mg(OH)$_2$ reduces the OH vacancy formation energy by about 60%, making it a promising method for a marked increase in the vacancy concentration. It is asserted that CO$_2$ adsorption energies and adsorption modes are strongly dependent on vacancy formation energy.[42] A lower vacancy formation energy, i.e., a larger vacancy concentration, would facilitate CO$_2$ adsorption. Therefore, it is expected that MgO–Mg(OH)$_2$ with interstitial C will exhibit higher CO$_2$ adsorption.

Carbon doping into the MgO–Mg(OH)$_2$ system lowers the vacancy formation energies in both phases, thereby providing additional basic sites for CO$_2$ capture. Notably, the presence of vacancy defects in the Mg(OH)$_2$ regions offers extra CO$_2$ adsorption sites, enabling Mg(OH)$_2$ to facilitate both CO$_2$ diffusion and adsorption in the carbon-doped MgO–Mg(OH)$_2$ nanocomposite. CO$_2$ capture is therefore governed by a combination of surface adsorption on MgO domains and interlayer-assisted adsorption on defect sites on exposed (001) Mg(OH)$_2$ basal planes. Interestingly, despite exhibiting a lower BET surface area than its undoped counterpart, the carbon-doped MgO–Mg(OH)$_2$ nanocomposite achieved significantly higher CO$_2$ uptake. Although the carbon-doped sample exhibits a lower BET surface area (46.4 vs. 62.3 m^2 g^{-1}), its much higher defect density and vacancy concentration provide chemically stronger binding sites for CO$_2$ molecules. It is reported that main chemisorption sites for CO$_2$ are under-coordinated surface oxygen atoms and oxygen vacancy defects.[43,44] Therefore, these findings indicate that the improved CO$_2$ capture performance is strongly governed by defect-driven surface chemistry introduced through carbon incorporation in the binary system
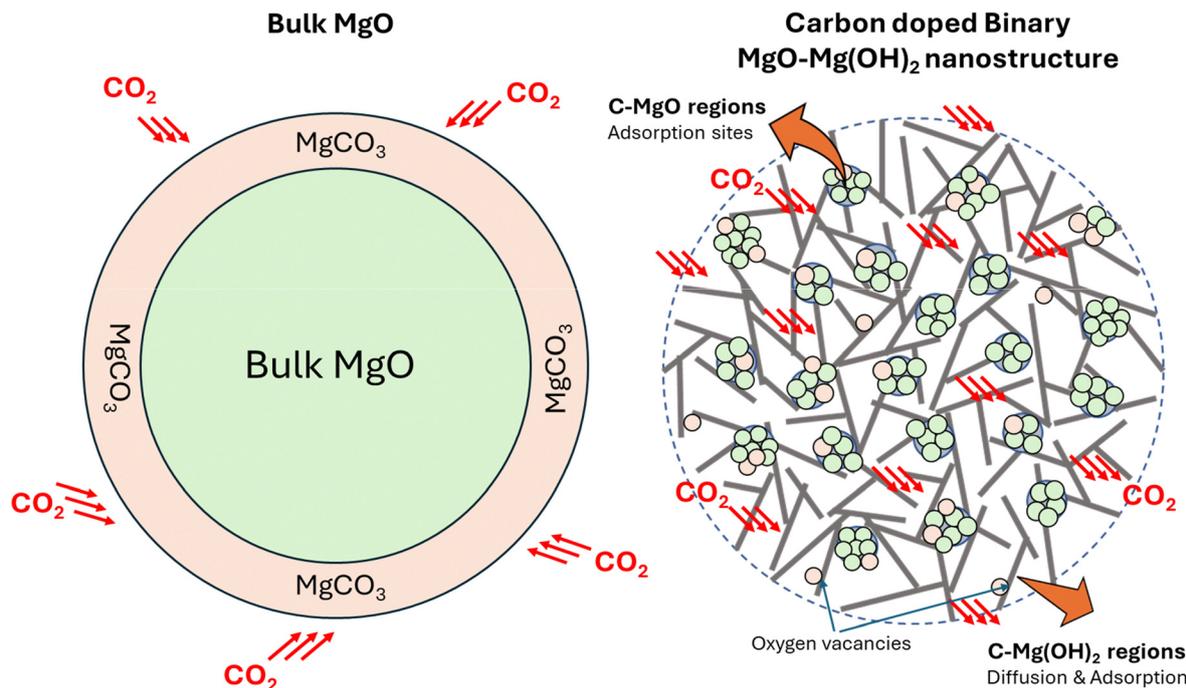
Fig. 8 Schematic illustration of the CO_2 adsorption mechanism in carbon-doped binary $MgO–Mg(OH)_2$ nanocomposites in comparison to bulk MgO.

rather than being purely dependent on the surface area. The proposed CO_2 adsorption mechanism for the carbon-doped $MgO–Mg(OH)_2$ nanocomposite is schematically illustrated in Fig. 8. These observations are consistent with reported experimental and theoretical studies demonstrating that dopant-induced oxygen vacancies act as dominant active sites for CO_2 chemisorption on MgO and related metal oxides.[38,43,45–50]

Therefore, our findings demonstrate a new binary strategy that minimizes the carbonate blocking effect in MgO by utilizing dual function carbon doped $Mg(OH)_2$ regions that facilitate both CO_2 diffusion and adsorption. Additionally, carbon doped MgO regions further facilitate enhanced CO_2 adsorption in comparison to undoped MgO. While interstitial carbon doping in Mg-based oxides is typically energetically demanding, the layered morphology and defect landscape generated by spray drying could enable low-energy entrapment of carbon species.

4. Conclusions

In summary, this work presents a dual-function CO_2 sorbent design based on carbon-doped $MgO–Mg(OH)_2$ nanoparticles synthesized *via* a non-equilibrium spray drying process. The resulting nanocomposite overcomes two fundamental challenges in MgO-based sorbents: carbonate passivation and inefficient Mg utilization. By engineering a carbon-doped $Mg(OH)_2$ interface, we enable concurrent suppression of $MgCO_3$ formation and additional CO_2 adsorption activity through defect-induced surface basicity.

While the conversion of MgO to $Mg(OH)_2$ typically reduces the active CO_2-philic content, carbon doping restores and

enhances functionality by introducing oxygen vacancies and increasing CO_2-affinitive sites across both MgO and $Mg(OH)_2$ domains. The rapid kinetics of spray drying facilitate carbon entrapment near the particle surface, yielding a self-limiting, carbon-rich $Mg(OH)_2$ region that mimics carburization behavior and forms an effective CO_2-selective interface.

XRD analysis confirmed the presence of highly oriented flake-like $Mg(OH)_2$ structures, characterized by a dominant (001) reflection and anisotropic peak intensity decay—features consistent with the 2D-layered morphology and potential interlayer carbon enrichment. First-principles calculations further support the observed performance enhancement, showing that interstitial carbon lowers the formation energy of oxygen and hydroxyl vacancies, thereby increasing defect densities and CO_2 binding potential.

The optimized composite achieved a CO_2 uptake of 5.45 wt% at room temperature with a low regeneration temperature of 150 °C. Remarkably, this performance was achieved despite a lower surface area than the undoped sample, highlighting the pivotal role of carbon-doped $Mg(OH)_2$ as both a CO_2 barrier and an active capture phase. It is important to note that only a fixed precursor concentration was investigated in this work. While the present results clearly establish the beneficial role of carbon incorporation, systematic variation of precursor loading could provide a more detailed correlation between the carbon content, defect density, and CO_2 adsorption. While the present study demonstrates stable CO_2 capture performance over six adsorption–desorption cycles, extended long-cycle durability remains an important aspect for future investigation. This kinetically formed, dual-function interface offers a new route toward efficient, scalable, and regenerable solid sorbents for carbon capture applications.

Author contributions

Hashan N. Thenuwara: methodology, investigation, validation, and writing – original draft. W. P. Cathie Lee: methodology and writing – review and editing. Shunnian Wu: investigation, validation and writing – original draft. Sim Jia Yu: investigation. Siew Yee Wong: investigation. Xu Li: conceptualization, resources, and supervision. Ping Wu: conceptualization, resources, supervision, writing – review and editing, project administration, and funding acquisition.

Conflicts of interest

The authors declare no competing interest.

Data availability

Data will be made available on request.

Supplementary information (SI) is available. See DOI: https://doi.org/10.1039/d5ma01199j.

Acknowledgements

References

1 IPCC, Climate Change 2014: Synthesis Report. Contribution of Working Groups I, II and III to the Fifth Assessment Report of the Intergovernmental Panel on Climate Change, 2014.
2 J. P. Smol, *Nature*, 2012, **483**, S12–S15.
3 R. S. Haszeldine, *Science*, 2009, **325**, 1647–1652.
4 H. H. Khoo, P. N. Sharratt, J. Bu, T. Y. Yeo, A. Borgna, J. G. Highfield, T. G. Björklöf and R. Zevenhoven, *Ind. Eng. Chem. Res.*, 2011, **50**, 11350–11357.
5 C. Ma, F. Pietrucci and W. Andreoni, *J. Chem. Theory Comput.*, 2015, **11**, 3189–3198.
6 H. A. Patel, J. Byun and C. T. Yavuz, *ChemSusChem*, 2017, **10**, 1303–1317.
7 P. Luis, *Desalination*, 2016, **380**, 93–99.
8 Y. Hu, Y. Guo, J. Sun, H. Li and W. Liu, *J. Mater. Chem. A*, 2019, **7**, 20103–20120.
9 C. L. Wetteland, J. de Jesus Sanchez, C. A. Silken, N.-Y. T. Nguyen, O. Mahmood and H. Liu, *J. Nanopart. Res.*, 2018, **20**, 215.
10 F. Donat and C. R. Müller, *Curr. Opin. Green Sustainable Chem.*, 2022, **36**, 100645.
11 Y.-C. Hsu, S. Wu, J.-Y. Chiu, H. N. Thenuwara, H. L. Senevirathna and P. Wu, *Materials*, 2023, **16**(19), 6533.
12 W. Gao, T. Zhou, Y. Gao, B. Louis, D. O'Hare and Q. Wang, *J. Energy Chem.*, 2017, **26**, 830–838.
13 H. L. Senevirathna, S. Wu, W. P. C. Lee and P. Wu, *Materials*, 2022, **15**(2), 680.
14 S. Wu, W. P. C. Lee, H. N. Thenuwara, X. Li and P. Wu, *Biomimetics*, 2025, **10**(1), 9.
15 H. N. Thenuwara, H.-J. Shih, H. L. Senevirathna, Y.-C. Lee, X. Li and P. Wu, *ACS Appl. Electron. Mater.*, 2025, **7**, 831–837.
16 H. L. Senevirathna, S. Wu, W. C. Lee and P. Wu, *Materials*, 2022, **15**, 680.
17 H. L. Senevirathna, S. Wu, C. Lee, J. Y. Kim, S. S. Kim, K. Bai and P. Wu, *RSC Adv.*, 2023, **13**, 27946–27955.
18 A. Agarwal, H. N. Thenuwara and P. Wu, *Sustainable Energy Fuels*, 2024, **8**(21), 5041–5049.
19 G. Kresse and J. Furthmuller, *Phys. Rev. B:Condens. Matter Mater. Phys.*, 1996, **54**, 11169–11186.
20 B. Hammer, L. B. Hansen and J. K. Norskov, *Phys. Rev. B:Condens. Matter Mater. Phys.*, 1999, **59**, 7413–7421.
21 G. Kresse and D. Joubert, *Phys. Rev. B:Condens. Matter Mater. Phys.*, 1999, **59**, 1758–1775.
22 G. Kresse and J. Furthmuller, *Comput. Mater. Sci.*, 1996, **6**, 15–50.
23 S. Grimme, J. Antony, S. Ehrlich and H. Krieg, *J. Chem. Phys.*, 2010, **132**, 19.
24 H. J. Monkhorst and J. D. Pack, *Phys. Rev. B*, 1976, **13**, 5188–5192.
25 S. Wu, B. T. Tan, H. L. Senevirathna and P. Wu, *Appl. Surf. Sci.*, 2021, **562**, 150187.
26 S. Wu, W. P. C. Lee, H. N. Thenuwara and P. Wu, *Nanomaterials*, 2025, **15**(5), 370.
27 L. Stobinski, B. Lesiak, A. Malolepszy, M. Mazurkiewicz, B. Mierzwa, J. Zemek, P. Jiricek and I. Bieloshapka, *J. Electron Spectrosc. Relat. Phenom.*, 2014, **195**, 145–154.
28 J. Kim, E. Yamasue, H. Okumura, K. N. Ishihara and C. Michioka, *J. Alloys Compd.*, 2016, **685**, 135–141.
29 H. Sun, H. Liu, Z. Hou, R. Zhou, X. Liu and J.-G. Wang, *Chem. Eng. J.*, 2020, **387**, 124204.
30 F. Zhang, H. Zhang and Z. Su, *Appl. Surf. Sci.*, 2007, **253**, 7393–7397.
31 S. Sikdar, A. Ghosh and R. Saha, *Environ. Sci. Pollut. Res.*, 2020, **27**, 17738–17753.
32 M. Subash, M. Chandrasekar, S. Panimalar, C. Inmozhi, K. Parasuraman and R. Uthrakumar, *Biomass Convers. Biorefin.*, 2022, **13**, 3427–3437.
33 A. Agarwal, H. L. Senevirathna, S. H. Koo, C. S. L. Wong, T. S. K. Lim, F. C. Ng, F. Anariba and P. Wu, *Sci. Rep.*, 2023, **13**(1), 13290.
34 M. Kuang, Y. Shang, G. Yang, B. Liu and B. Yang, *Environ. Sci. Pollut. Res.*, 2019, **26**, 18825–18833.
35 M. H. Zahir, M. M. Rahman, K. Irshad and M. M. Rahman, *Nanomaterials*, 2019, **9**(12), 1773.
36 A. H. Ruhaimi, M. A. A. Aziz and A. A. Jalil, *J. CO$_2$ Util.*, 2021, **43**, 101357.
37 J. I. Di Cosimo, V. K. Díez, C. Ferretti and C. R. Apesteguía, in *Catalysis*, ed. J. Spivey, K. M. Dooley and Y.-F. Han, The Royal Society of Chemistry, 2014, vol. 26.
38 U. J. Etim, C. Zhang and Z. Zhong, *Nanomaterials*, 2021, **11**(12), 3265.

39 X.-H. Zhao, Q.-S. Chen, D.-H. Zhuo, J. Lu, Z.-N. Xu, C.-M. Wang, J.-X. Tang, S.-G. Sun and G.-C. Guo, *Electrochim. Acta*, 2021, **367**, 137478.

40 X. Yan, C. Duan, S. Yu, B. Dai, C. Sun and H. Chu, *J. CO$_2$ Util.*, 2024, **79**, 102648.

41 R. Khokhra, B. Bharti, H.-N. Lee and R. Kumar, *Sci. Rep.*, 2017, **7**, 15032.

42 Y. Hinuma, T. Toyao, T. Kamachi, Z. Maeno, S. Takakusagi, S. Furukawa, I. Takigawa and K. Shimizu, *J. Phys. Chem. C*, 2018, **122**, 29435–29444.

43 E. Florez, P. Fuentealba and F. Mondragón, *Catal. Today*, 2008, **133**, 216–222.

44 G. Pacchioni, *Surf. Sci.*, 1993, **281**, 207–219.

45 Z. Zhu, X. Shi, Y. Rao and Y. Huang, *Chin. Chem. Lett.*, 2024, **35**, 108954.

46 K. Kumar, A. Dhasmana, S. Mishra, R. Sharma, N. H. de Leeuw, J. Adam and A. K. Mishra, *Mater. Today Commun.*, 2025, **46**, 112907.

47 L. Wang, Y. Yao, T. Tran, P. Lira, S. Sternberg P.E, R. Davis, Z. Sun, Q. Lai, S. Toan, J. Luo, Y. Huang, Y. H. Hu and M. Fan, *J. Environ. Manage.*, 2023, **332**, 117398.

48 J. Niu, C. Zhang, H. Liu, Y. Jin and R. Zhang, *Front. Energy*, 2023, **17**, 545–554.

49 S. Hussain, L. Zhang, Z. Xie, J. Yang and Q. Li, *Phys. Chem. Chem. Phys.*, 2024, **26**, 29328–29338.

50 L. Liu, W. Fan, X. Zhao, H. Sun, P. Li and L. Sun, *Langmuir*, 2012, **28**, 10415–10424.